Journal of Colloid and Interface Science 585 (2021) 480–489

Contents lists available at ScienceDirect

Journal of Colloid and Interface Science

journal homepage: www.elsevier.com/locate/jcis

Regular Article

Controlled morphology and dimensionality evolution of NiPd bimetallic nanostructures

Mai Maize [a,b,c], Hanaa A. El-Boraey [a], Mohamed I. Ayad [a], Justin D. Holmes [b,c], Gillian Collins [b,c,*]

[a] Department of Chemistry, Faculty of Science, Menoufia University, Shebin El-Kom 32512, Egypt
[b] School of Chemistry and Tyndall National Institute, University College Cork, Cork T12 YN60, Ireland
[c] AMBER Centre, Environmental Research Institute, University College Cork, Cork T23 XE10, Ireland

HIGHLIGHTS

- Versatile NiPd nanostructures prepared via one-pot aqueous synthesis.
- HCl concentration and reaction aging time plays vital role in the morphology evolution.
- The diverse NiPd nanostructures exhibit enhanced catalytic activity toward the reduction of 4-nitrophenol.

GRAPHICAL ABSTRACT

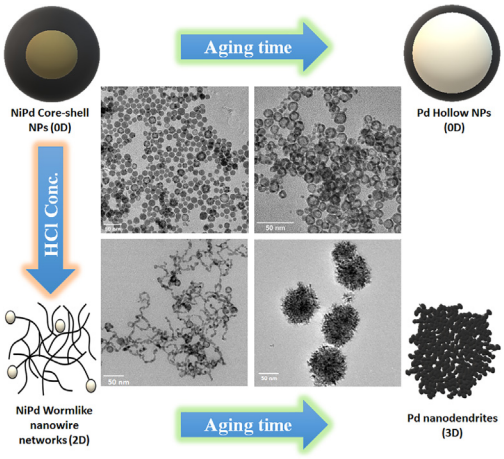

ARTICLE INFO

Article history:
Received 1 September 2020
Revised 29 September 2020
Accepted 8 October 2020
Available online 13 October 2020

Keywords:
NiPd bimetallic nanoparticles
Shape control
Structural evolution
Core-shell structure
Hollow structure
Nanowire network structure
Dendritic structure
Reaction mechanism
Catalysts
4-nitrophenol

ABSTRACT

Controlling the morphology of noble metal-based nanostructures is a powerful strategy for optimizing their catalytic performance. Here, we report a one-pot aqueous synthesis of versatile NiPd nanostructures at room temperature without employing organic solvents or surfactants. The synthesis can be tuned to form zero-dimensional (0D) architectures, such as core–shell and hollow nanoparticles (NPs), as well as nanostructures with higher dimensionality, such as extended nanowire networks and three-dimensional (3D) nanodendrites. The diverse morphologies were successfully obtained through modification of the HCl concentration in the Pd precursor solution, and the reaction aging time. An in-depth understanding of the formation mechanism and morphology evolution are described in detail. A key factor in the structural evolution of the nanostructures was the ability to tune the reduction rate and to protonate the citrate stabiliser by adding HCl. Spherical core–shell NPs were formed by the galvanic replacement-free deposition of Pd on Ni NPs which can be transformed to hollow NPs *via* a corrosion process. High concentrations of HCl led to the transition of isotropic spherical NPs into anisotropic wormlike nanowire networks, created through an oriented attachment process. Aging of these nanowire networks resulted in the formation of 3D porous nanodendrites *via* a corrosion process. The diverse structures of NiPd NPs were anchored onto acid treated-activated carbon (AC) and exhibited improved catalytic efficiency towards the hydrogenation of 4-nitrophenol (4-NP) to 4-aminophenol (4-AP).

* Corresponding author at: School of Chemistry and Tyndall National Institute, University College Cork, Cork T12 YN60, Ireland.
E-mail addresses: j.holmes@ucc.ie (J.D. Holmes), g.collins@ucc.ie (G. Collins).

https://doi.org/10.1016/j.jcis.2020.10.030
0021-9797/

1. Introduction

Metal nanoparticles (NPs) have garnered sustained research interest because of their unique physical and chemical properties that can be controlled and optimized by altering their size, shape, composition, crystal structure, or surface functionality [1–3]. Noble metal NPs such as Pd are employed in a myriad of catalytic applications, including hydrogenations [4], oxidations [5], organic coupling reactions [6] and electrochemical reactions [7]. The limited natural reserves and cost associated with extracting Pd from the ground has led to the tremendous use of bimetallic noble metal NPs in catalytic applications, as noble metals can be combined with less expensive transition metals without affecting catalytic performance.

Bimetallic nanostructures often display remarkably improved catalytic activity and selectivity compared to their monometallic counterparts due to the synergistic effects between the constituent metals [8–10]. In particular, alloying Pd with non-precious first-row transition metals, such as Ni, Co, and Fe can lead to cost-effective catalysts and enables modification of the electronic and geometric structures for enhanced activity and/or selectivity. NiPd NPs have shown exceptional activity and stability towards a range of coupling reactions [11–13], and the oxygen reduction reaction (ORR) [14,15]. PdNi [16] and PdCu NPs [17] have also displayed superior performance in the oxidation of formic acid compared to monometallic Pd NPs.

In addition to alloying, the morphology of bimetallic NPs can be tailored with specific crystal facets to maximize the number of low co-ordinate atom at corner, edge and defect sites, enhancing their reactivity [18–21]. Generally, the final shape of NPs can be controlled by manipulating thermodynamic and/or kinetic parameters [22]. Most bimetallic NP catalysts produced to-date are either isotropic spherical nanostructures, such as core–shell [23,24], or hollow structures [14,16,25]. However, the deposition of a noble metal with a high reduction potential, e.g. Pd, on the surface of another metal with a lower reduction potential remains challenging due to galvanic replacement reactions (GRRs), which can result in unwanted hollow structures, such as nanorings and nanocages [26,27]. Through careful control of reaction thermodynamics and kinetics, GRRs can be suppressed to produce only core–shell structures [3,28,29]. Engineered hollow nanostructures have however displayed impressive performances as electrocatalysts, photocatalysts and biocatalysts [30].

In addition to traditional zero-dimensional nanostructures, the use of two- and three-dimensional nanostructures such as nanowire networks and nanodendrites, have become popular for catalytic applications; having geometries with an abundance of surface defect atoms [31]. To date, the development of NiPd structures such as nanowire networks [32,33], or nanodendrites [34] often require multistep reactions in the presence of pre-synthesized seeds, harsh experimental conditions, organic solvents, or surfactants that are environmentally unfriendly and which can cause catalyst deactivation. Subsequently, developing a facile and efficient approach to construct different Pd bimetallic nanostructures with high catalytic activity represents a great challenge.

Here, we present a synthetic protocol for fabricating a variety of NiPd nanostructures *via* a one-pot wet chemical method in aqueous solution at room temperature without the presence of surfactant. The method allows the morphology of the NPs to be tuned from zero-dimensional (0D) core–shell and hollow nanostructures to two-dimensional (2D) nanowire networks and three-dimensional (3D) nanodendrites. A systematic investigation into the mechanism demonstrates that altering the HCl concentration in the Pd precursor (H_2PdCl_4) solution and the aging time of the NPs enables different reaction pathways to be selected thereby allowing tuning of the final nanostructure morphology. The synthesized structures of NiPd NPs were supported on acid-treated activated carbon and their catalytic efficiency was validated over the reduction of toxic 4-nitrophenol (4-NP) to eco-friendly 4-aminophenol (4-AP).

2. Experimental

2.1. Materials

Trisodium citrate dihydrate ($Na_3C_6H_5O_7{\cdot}2H_2O$, 99%), sodium borohydride ($NaBH_4$, 99.99%), palladium(II) chloride ($PdCl_2$, 99.9%), sodium palladium(II) tetrachloride (Na_2PdCl_4, 98%), cobalt (II) chloride hexahydrate ($CoCl_2{\cdot}6H_2O$, ≥99%), Iron(III) chloride ($FeCl_3$, ≥99%), copper(II) chloride dihydrate ($CuCl_2{\cdot}2H_2O$, ≥99.95%), hydrochloric acid (HCl, 37%), nitric acid (HNO_3, 65%), sodium hydroxide (NaOH, 98%), commercial Pd/C (5 wt%) and 4-nitrophenol ($O_2NC_6H_4OH$, 98%) were purchased from Sigma-Aldrich. Nickel(II) chloride hexahydrate ($NiCl_2{\cdot}6H_2O$, 99.95%) was obtained from Alfa Aesar. All chemicals were of analytical grade and used as received without further purification. Activated charcoal (untreated powder; 100–400 mesh) was purchased from Honeywell FlukaTM. Deionized water (DI H_2O) was used as the solvent. All glassware and magnetic stir bars were cleaned with aqua regia, followed by rinsing with DI H_2O before drying in an oven.

2.2. Synthesis

A one-pot synthesis was used to fabricate the NiPd bimetallic NPs. Firstly, the sacrificial Ni NPs were synthesized using the borohydride reduction method. Briefly, in a two-necked 100 mL round bottom flask, 4.7 mg of $NiCl_2{\cdot}6H_2O$ (0.02 mmol), and 29.4 mg of trisodium citrate (TSC) (0.1 mmol) were dissolved in 40 mL of DI H_2O at room temperature (~20 °C). The solution was stirred and purged with N_2 for 30 min to eliminate the dissolved O_2. Then, 2 mL of freshly prepared aqueous $NaBH_4$ solution (7.5 mg) was added dropwise into the solution under magnetic stirring at 550 rpm. The appearance of a dark yellow color in the solution indicated the formation of Ni NPs. After 10 min, 40 mL of H_2PdCl_4 solution (0.02 mmol) was injected into the Ni NPs with a rate of 1.4 mL/min at room temperature. The reaction mixture was allowed to stir for another 3 h. To validate the critical role of the aging time, the colloidal solutions of NPs were stored for 24 h under ambient conditions (air, ~20 °C) without any agitation. For comparison, the same procedure was done using Na_2PdCl_4 (0.02 mmol) solution as a Pd precursor without extra HCl addition, while other conditions were kept unvaried. For Co-Pd, Fe-Pd, and Cu-Pd systems, the same protocol was used except replacing $NiCl_2{\cdot}6H_2O$ with $CoCl_2{\cdot}6H_2O$, $FeCl_3$, and $CuCl_2{\cdot}2H_2O$, respectively with the same molar amount.

2.2.1. Preparation of H_2PdCl_4 solution (0.02 mmol)

Stock solutions of 10 mM H_2PdCl_4 were prepared by dissolving 88.65 mg of $PdCl_2$ in 50 mL of a 0.2 M, 0.1 M and 0.02 M HCl. H_2PdCl_4 solutions (0.02 mmol) were prepared by diluting 2 mL of stock solutions to 40 mL with DI·H_2O to give 0.02 mmol H_2PdCl_4/10 mM HCl solution, 0.02 mmol H_2PdCl_4/5 mM HCl and 0.02 mmol H_2PdCl_4/1 mM HCl solutions, respectively.

2.3. Immobilization of NiPd NPs on acid-treated activated carbon

For improving the absorbing ability of activated carbon (AC), it was treated with HNO_3 acid. 1 g of AC was refluxed in 10 mL of 6 M HNO_3 solution while stirring for 6 h at 95 °C. The AC was collected by centrifuge and washed until neutral pH of the filtrate.

To immobilize the NPs, the AC was added to the as-prepared NPs solution and sonicated for 10 min. The mixture was stirred at room temperature for 2 h and collected by centrifugation. The catalyst was washed with DI water and acetone several times to remove the residual impurities and then dried at 50 °C overnight.

2.4. Characterization

Microscopy. Low-resolution transmission electron microscopy (TEM) images were recorded using a JEOL 2100 transmission electron microscope operated at 200 kV. High-resolution (HR)TEM images, scanning transmission electron microscopy (STEM), and energy dispersive X-ray spectroscopy (EDX) mapping and line scanning were performed on the FEI Titan transmission electron microscope at an operating voltage of 300 kV. For electron microscopy grids, as-prepared NPs solution was directly dropped on a carbon-coated Cu grid (300 mesh, Agar Scientific), followed by drying under ambient condition (air, ~20 °C). *X-ray Photoelectron Spectroscopy (XPS)* was carried out using a KRATOS AXIS ULTRA spectrometer equipped with an Al Kα (hν = 1486.58 eV) X-ray source. All spectra were calibrated using the C 1s peak at 284.8 eV. *Inductively coupled plasma optical emission spectroscopy (ICP-OES)* was conducted for determining the accurate amounts of metals deposited on the AC support using Varian 710-ES ICP Optical Emission Spectrometer. Working parameter: the power of 1 kW with the auxiliary of 1.5 L/min and nebuliser pressure of 200 kPa. The emission lines used to measure the Ni and Pd concentrations were 231.604 nm and 340.458 nm, respectively. The microwave-assisted digestion method using nitric acid and hydrogen peroxide was performed to prepare the samples for the ICP measurements. *UV–Vis spectroscopy* was performed for observing the catalytic reduction of 4- nitrophenol using Genesys 10 s UV–Vis Thermo scientific spectrometer.

2.5. Catalytic evaluation of nanostructures

The catalytic reduction of 4-nitrophenol (4-NP) was chosen as a model reaction to assess the catalytic efficiency of NiPd nanoparticles with different morphologies and commercial Pd/C. Due to the low solubility of 4-NP in water, 4-NP was first dissolved in NaOH. The resulting 4-nitrophenolate ion was then reduced by $NaBH_4$ in the presence of the catalyst. Reactions were performed in a cuvette as follows: typically, freshly prepared aqueous solutions of 4-NP (0.06 mM; 3 mL) and $NaBH_4$ (0.025 M; 300 μL) were mixed with 1 mg of the catalyst. The progress of the 4-nitrophenolate ion conversion to 4-aminophenol (4-AP) was monitored by UV–Vis spectrometer by recording the absorption spectra of the reaction mixture with a 30 s time intervals at ambient temperature.

3. Results and discussion

Fig. 1 illustrates the shape evolution of NPs upon the addition of a H_2PdCl_4/5 mM HCl solution to a solution of Ni NPs. Fig. 1A shows that TEM analysis of NPs after 3 h had a predominately solid spherical morphology. Detailed size distribution analysis showed a bimodal diameter distribution with modes centered at 5.5 and 15.7 nm (Fig. S1A). In addition, there was a minor contribution of hollow spheres with a diameter of 19.1 ± 3.4 nm (Fig. S1B) and a shell thickness of 4.3 ± 1.8 nm (Fig. S1C). EDX mapping and line scans of the solid NPs (15.7 nm), shown in Fig. 1(B, C), indicate that they consist of a core–shell structure. The typical chemical composition of the NPs, as determined by EDX analysis showed a Ni core with monometallic Pd located in the shell. This core–shell structure was also evidenced by XPS analysis, displayed in Fig. S2A, which showed no peaks for the Ni 2p core level due to their attenuation from the Pd overlayer. EDX analysis (Fig. S3) confirmed that the smaller diameter NPs (5.5 nm) were composed of Pd only, attributed to a minor degree of homogeneous nucleation of Pd. Fig. 1D shows the morphological evolution of the core–shell NPs to a hollow nanostructure on aging the solution for 24 h due to etching of the Ni core. The mean diameter of the hollow nanospheres was determined to be 14.4 ± 2.4 nm (Fig. S4A) with a shell thickness of 2.5 ± 0.5 nm (Fig. S4B). EDX mapping and line scans of the hollow nanospheres (Fig. 1(E, F)) confirm etching of the Ni core to leave a shell consisting mostly of Pd with an estimated composition of Ni_4Pd_{96}, also supported by XPS analysis (Fig. S2A), however, it could not be quantified accurately due to detection limits. HRTEM analysis of the hollow NPs (the inset of Fig. 1D) reveals the lattice fringe with a d spacing of 0.234 nm, matching the (1 1 1) plane of face-centered cubic Pd [35].

Conducting the same synthesis procedure at a lower pH by using a H_2PdCl_4/10 mM HCl solution allows assess to nanostructures with 2D and 3D architectures. After 3 h, Fig. 2A shows the formation of 2D wormlike nanowire networks. Despite being overlapped, folded and twisted, these nanowire networks were well dispersed, highly interconnected and extended to hundreds of nanometers in length as observed in low-resolution TEM (Fig. S5A). The typical diameter of the wormlike nanowire was 5.6 ± 1.1 nm (Fig. S5B) and displayed excellent uniformity throughout the nanowire networks. These nanowire networks are potentially highly effective catalysts due to their inherent anisotropic structures and the reactivity of the surface atoms at the different facets. Some of these nanowires were connected with a hollow head forming a tadpole structure. TEM analysis of an individual nanowire showed that they consisted of a polycrystalline assembly of nanoparticles made up of nodes (marked by circles in Fig. 2B) connected through slightly narrower stems (marked by rectangles in Fig. 2B). High-resolution TEM and EDX were carried out to further understand the structure and composition of the nanowire-tadpole morphologies. EDX line scans, taken from various positions along the nanowire (Fig. 2D), revealed different chemical compositions in the stem and nodes of the nanowire. The mean alloy composition, detailed in Fig. 2E, shows that the stems contained a greater amount of Ni while the nodes were predominately Pd. The presence of Ni was also supported by the XPS analysis (Fig. S6), however, it could not be quantified accurately due to detection limits. HRTEM of a typical tadpole (Fig. 3) showed the lattice fringes of its head and tail (node) with a measured d-spacing of 0.23 nm, attributed to (1 1 1) plane of face-centered cubic (fcc) Pd.

When the solution of these nanowire networks was aged for 24 h under ambient conditions, a shape transition from wormlike nanowire networks to 3D nanodendrites was observed, as shown in Fig. 4A. These nanodendrites had a bimodal distribution with a mean particle diameter modes centered at 30 nm and 95.6 nm (Fig. S7). HRTEM analysis, shown in the inset of Fig. 4A, confirmed the polycrystalline, porous nature of the nanodendrites with a d-spacing of 0.233 nm, assigned to the (1 1 1) plane of Pd. EDX elemental mapping and line scans (Fig. 4(B, C)) revealed that the nanodendrites were composed of Pd with trace amounts of Ni, which was also supported by the XPS analysis (Fig. S6).

The Pd 3d core level of the core–shell, hollow, nanowire and nanodendrite morphologies supported on activated carbon are shown in Fig. 5. The nanostructures were composed primarily of metallic Pd(0) with the Pd $3d_{5/2}$ and Pd $3d_{3/2}$ doublet located at a binding energy of 335.7 and 341.0 eV, respectively. For the core–shell, hollow and nanowire network structures, there was a small yet clearly observable positive shift of ~0.15 eV in the B.E. of the Pd 3d doublet associated with the presence of Ni. This higher binding energy can be attributed to the presence of $Pd^{\delta+}$ species generated by charge transfer from Pd to Ni [14,36]. A minor degree of

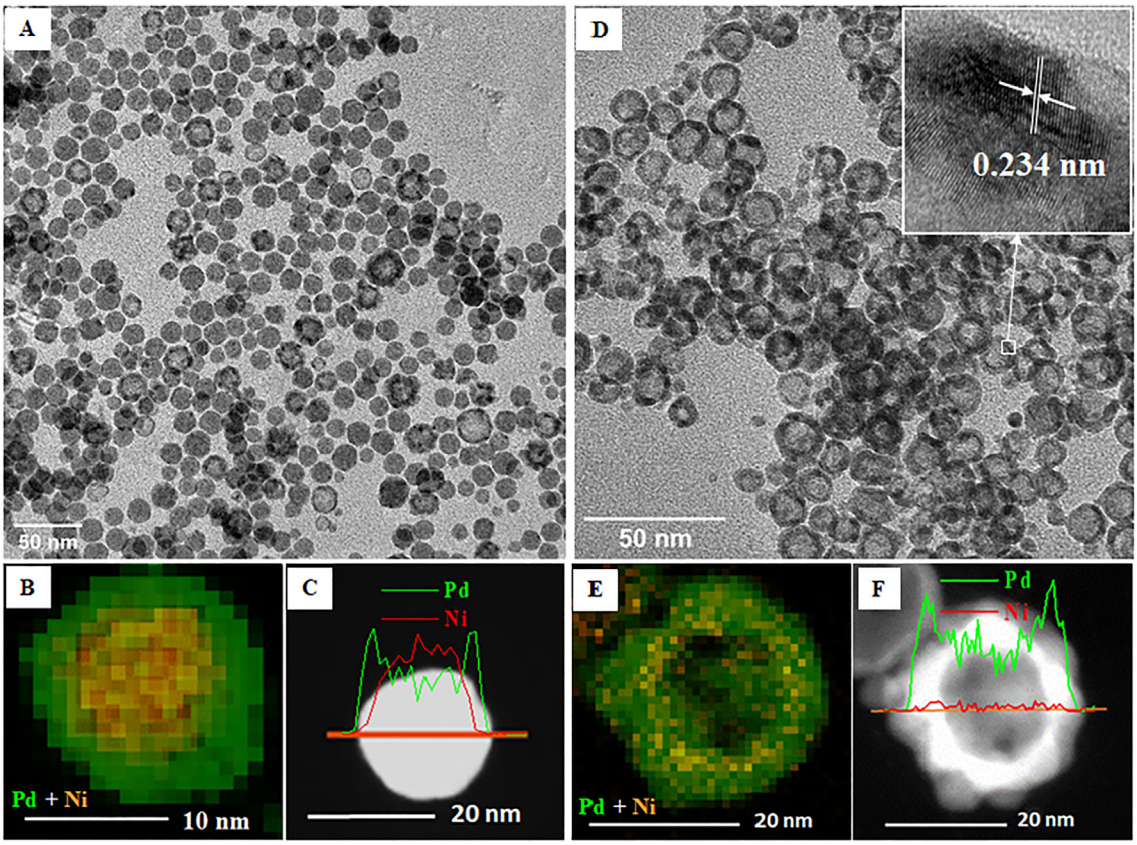

Fig. 1. (A) TEM images of NiPd core–shell NPs obtained from H_2PdCl_4/5 mM HCl after 3 h; (B) Elemental EDX mapping of solid NP [orange denotes Ni and green denotes Pd]; (C) EDX line scan of solid NP. (D) TEM images of NiPd hollow NPs obtained from H_2PdCl_4/5 mM HCl after aging for 24 h; the inset shows HR-TEM image of hollow NPs with the calculated lattice fringes for the shell; (E) Elemental EDX mapping of hollow NP [orange denotes Ni and green denotes Pd]; (F) EDX line scan of hollow NP. (For interpretation of the references to color in this figure legend, the reader is referred to the web version of this article.)

PdO_x species was also indicated by the presence of a peak at a binding energy of 337.8 eV.

3.1. Mechanism

The distinct change in the morphology of the NiPd NPs with varying HCl concentration in the H_2PdCl_4 solution suggests the essential role of HCl in the system. To further investigate the role of HCl concentration, the synthesis was carried out at a lower HCl concentration using a H_2PdCl_4/1 mM HCl solution. This HCl concentration yielded predominately small diameter partially agglomerated Pd NPs with a small contribution of hollow NPs, as shown in Fig. S8A formed through a GRR [14]. No core–shell NPs was observed using 1 mM HCl. After aging for 24 h, no significant shape transition was observed (Fig. S8B).

When the synthesis was performed using Na_2PdCl_4 as the precursor without the addition of HCl (Fig. S8C), small diameter NPs were exclusively observed, indicating that a suitable HCl concentration in addition to pH was a critical factor to tailor the structure of bimetallic NPs. To understand the pH-dependent reaction pathways occurring at different HCl concentrations, it is necessary to take into consideration the strong pH-dependent factors such as the reduction potential of $NaBH_4$ [37–39], Pd(II) complexes with chloride and/or hydroxide as the coordinating ligands [40–42], and the pH-dependent stabilizing ability of the trisodium citrate capping agent [43–45]. $NaBH_4$ is typically regarded as a strong reducing agent, however, its reducing capacity is strongly dependent on the solution pH with a redox potential of −0.48 V at pH 1 decreasing to −1.24 V vs. SHE at pH 14, therefore its reducing power is enhanced by decreasing pH [38,39]. The deprotonation and effectiveness of the stabilizer, trisodium citrate, is also pH-dependent. The pK_a values of citric acid; are 3.2, 4.8, and 6.4, respectively, therefore when the pH is above the third pK_a, the fully deprotonated Ct^{3-} is the dominating form of citrate. Decreasing the pH results in protonation of citrate ions thereby lowering its stabilizing ability.

The NiPd and Pd nanostructures synthesized under different solution pH and aging time are schematically shown in Scheme 1. Ni NPs were firstly synthesized through the redox reaction of the Ni salt and $NaBH_4$ forming a basic solution (pH = 9) due to the presence of $NaBH_4$. Oxidation of Ni NPs by the atmospheric oxygen was inhibited by bubbling the solution with N_2. The Pd precursor solution containing a certain concentration of HCl was injected into the Ni NPs and consequently, the pH of the solution gradually changes over the course of the reaction, as detailed in Table 1. Injection of the H_2PdCl_4 precursor into the Ni NPs solution gives rise to competing reactions involving Ni NPs or $NaBH_4$, and the rate of these competing reactions is controlled by tuning the solution pH. Using the H_2PdCl_4/1 mM HCl solution, the GRR of the Ni NPs dominates (with a rate of R_{gal}) to generate the hollow nanostructure (Pathway A, Scheme 1).

Using the H_2PdCl_4/5 mM HCl solution, the lower pH gives rise to a faster reduction of Pd(II) by $NaBH_4$ (with a rate of R_{red}). Galvanic replacement is quenched due to rapid reduction [28,29] and nucleation of Pd NPs which undergo deposition on the surface of the pre-existing Ni NPs generating core–shell NiPd nanostructures (Pathway B, Scheme 1). To investigate this growth mechanism, TEM analysis of the NPs formed at 15 min using different HCl

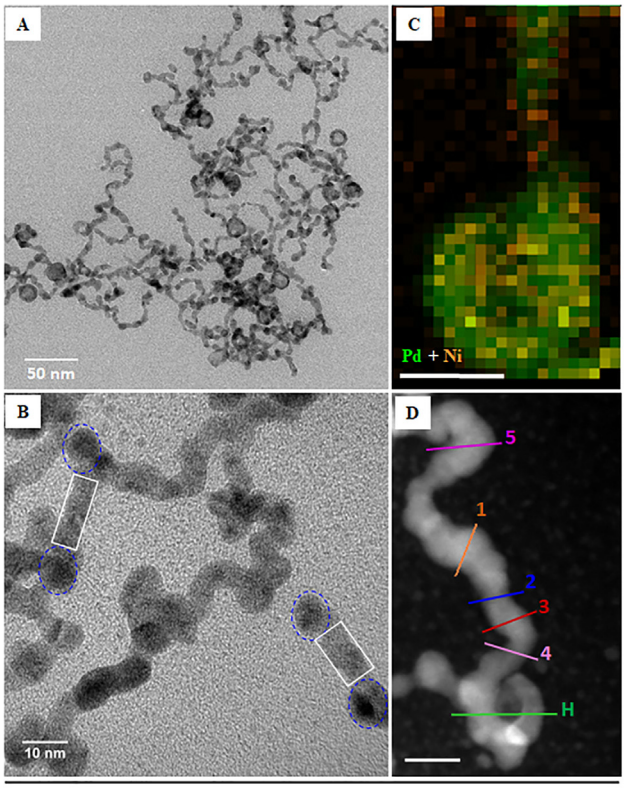

E

Element	Head			Tail		
	H	1 [Stem]	2 [Stem]	3 [Stem]	4 [Node]	5 [Node]
	At%	At%	At%	At%	At%	At%
Ni (K)	3.41	15.05	17.71	11.63	3.75	0.02
Pd (L)	96.59	84.95	82.29	88.37	96.25	99.98

Fig. 2. (A), (B) TEM images of NiPd wormlike nanowires-tadpoles obtained from H_2PdCl_4/10 mM HCl after 3 h. The blue dashed cycles represent the nodes while the white rectangles represent the stems. (C) Elemental EDX mapping of tadpole [orange denotes Ni and green denotes Pd]. (D), (E) EDX line scan of a tadpole. Scale bar in (C), (D) is 10 nm. (For interpretation of the references to color in this figure legend, the reader is referred to the web version of this article.)

concentrations was evaluated (Fig. S9). Analysis of the H_2PdCl_4/1 mM HCl solution confirmed galvanic replacement occurring at an early stage in the reaction (Fig. S9(A, B)). In contrast, TEM analysis of the H_2PdCl_4/5 mM HCl solution after 15 min (Fig. S9C) was dominated by the formation of solid NPs, supporting that the higher HCl concentration affected the reaction kinetics and blocked the galvanic reaction. This inhibition of GRR is attributed to the template surface passivation discussed by Gilroy et al [46].

Increasing the HCl concentration further using the H_2PdCl_4/10-mM HCl resulted in the transition from nanoparticle to wormlike nanowire networks and indicated a significant change in the growth mechanism. Two features are important when understanding the growth mechanism of these structures. Firstly, EDX identified the variable alloy composition of the nanowires having NiPd alloy segments and Pd segments. The lower pH of the solution resulted in the rapid reduction of the Pd precursor due to the higher reducing capacity of $NaBH_4$ at lower pH. This rapid reduction resulted in the formation of NiPd alloy NPs with the Ni NP seeds and homogeneously generated Pd nuclei. These NPs are ther-

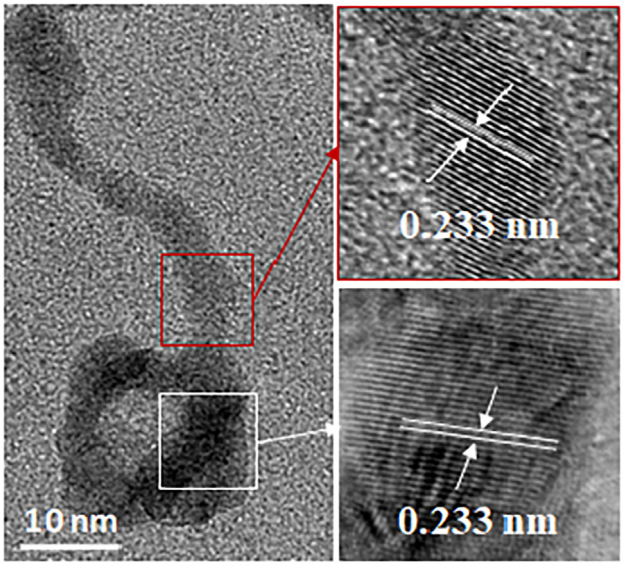

Fig. 3. TEM image and HR-TEM image of a tadpole with the calculated lattice fringes for the head and tail (node).

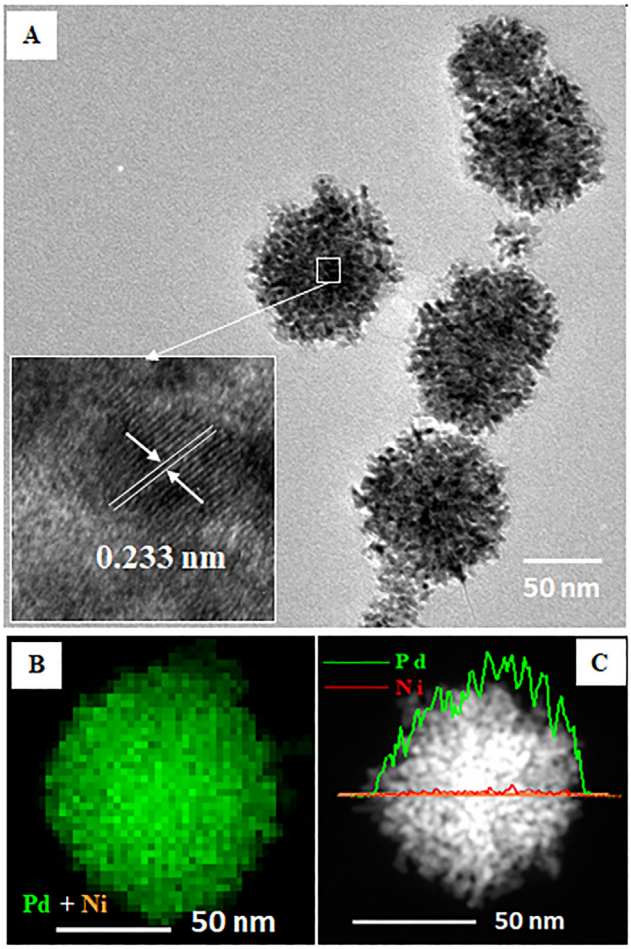

Fig. 4. (A) TEM images of Pd nanodendrites obtained from H_2PdCl_4/10 mM HCl after aging for 24 h. (B) Elemental EDX mapping of nanodendrite [orange denotes Ni and green denotes Pd]. (C) EDX line scan of nanodendrite. (For interpretation of the references to color in this figure legend, the reader is referred to the web version of this article.)

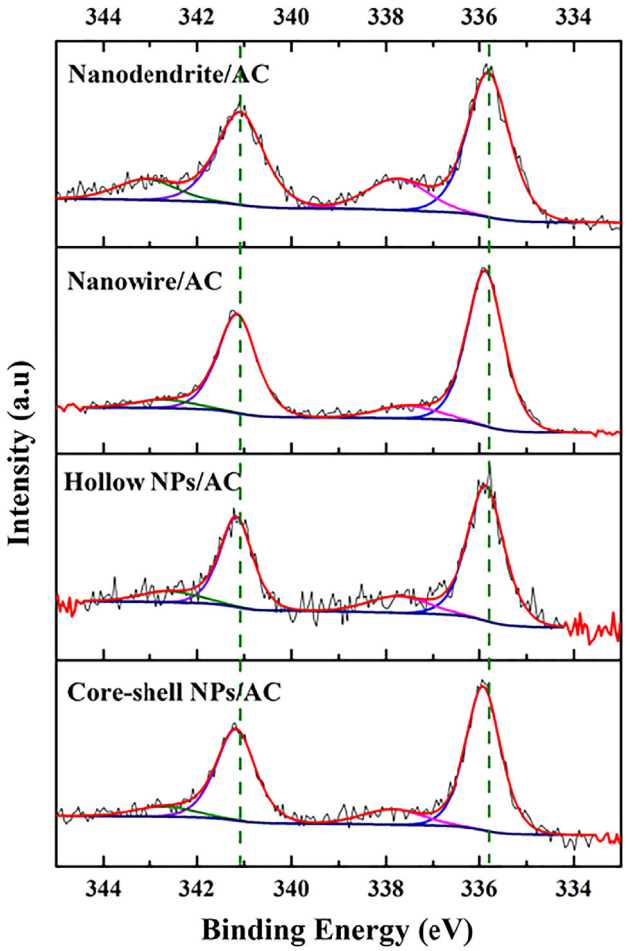

Fig. 5. Pd 3d XPS spectra of the four different nanostructures supported on activated carbon.

modynamically unstable and to minimise the total surface free energy of the system, nanowire networks grow through aggregation of NiPd NPs undergoing coalescence with homogeneous nucleated Pd NPs giving a nanowire with variable chemical composition as observed by EDX analysis (Pathway C, Scheme 1). Protonation of citrate capping agents at high HCl concentration weakens electrostatic repulsion of the capping agent promoting the attachment of the NPs [47]. Preferential adsorption of citrate on Pd {1 1 1} facets may also play a role in directing the anisotropic growth. The fast formation of nanowires was confirmed by TEM analysis 15 min after the addition of the H_2PdCl_4 solution (Fig. S10A). In order to validate the pivotal role of Ni on the formation of the nanowire networks, the synthesis was performed in the absence of the Ni seeds. TEM analysis, shown in Fig. S10B, illustrates the formation of Pd nanodendrites verifying that the presence of Ni seeds is necessary to drive the 2D growth of the wormlike nanowire networks. Previous studies on semiconductors [48] and metal nanowires [49–51] suggested the formation of dipolar moments and van der Waals attraction forces within the NPs as the driving force for the alignment of the small nanoparticles into nanowires. The formation of chains due to dipole–dipole attraction is quite plausible due to the presence of both NiPd and homogeneously nucleated Pd NPs present in solution, giving rise to different reactivity on the crystallographic surfaces. The second important feature in the wormlike nanowire networks is the presence of the tadpole nanostructures, these structures likely form early in the reaction where more basic pH conditions favour the GRR. The presence of hollow and solid tadpole heads and short nanowire tails was observed by TEM analysis after 15 min (Fig. S10A). As the pH decreased with the further addition of the Pd precursor, the enhanced reduction capacity of $NaBH_4$ led to the rapid reduction and nucleation of Pd NPs. The faster reduction kinetics coupled with the lower stabilizing power of the citrate resulted in the formation of nanowire networks through unidirectional aggregation.

In addition to the solution pH, the aging time was another essential parameter in influencing the shape evolution of the nanostructures. Upon aging the NiPd core–shell NPs, Cl^- ions could

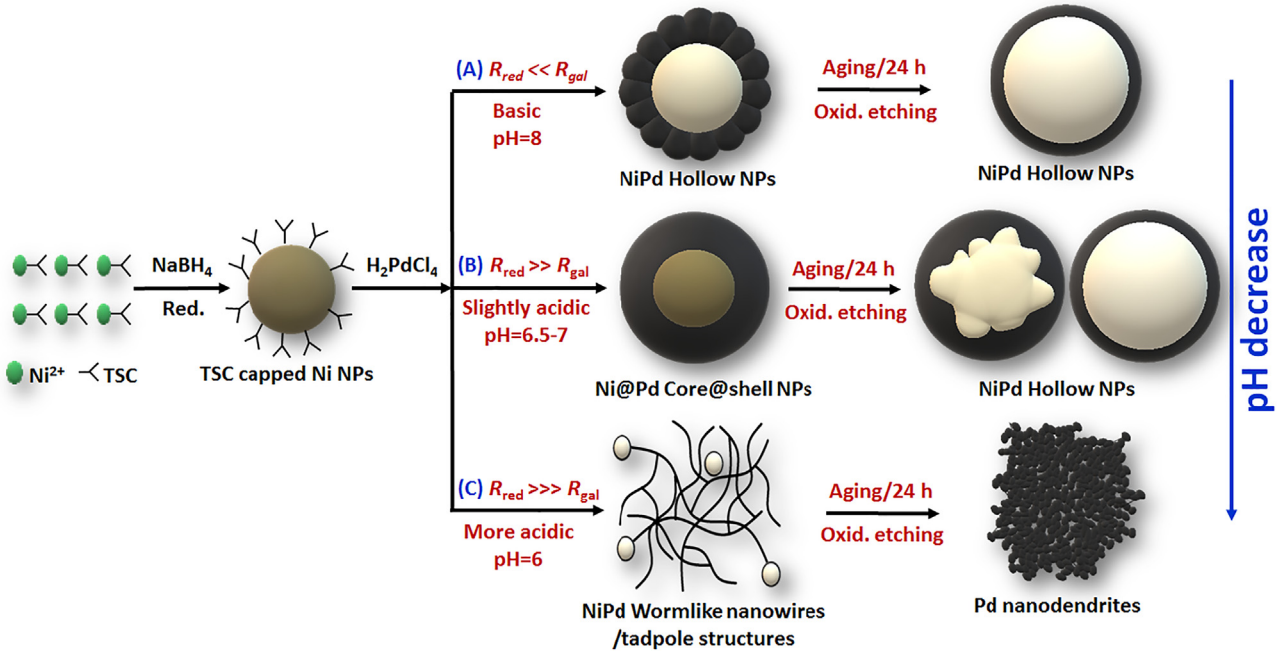

Scheme 1. Schematic illustrating the synthesis of NiPd bimetallic NPs and the structure evolution relying on the solution pH and aging time via; (A) galvanic reaction route, (B) seeded growth route, and (C) crystallite coalescence route.

Table 1
Solution pH levels and citrate ion formed during the reaction.

HCl Conc. in H_2PdCl_4	Solution pH			Citrate ion form [44]
	1	2	3	B/A
1 mM	7	9	8	Ct^{3-}/Ct^{3-}
5 mM	7	9	6.5–7	Ct^{3-}/HCt^{2-}
10 mM	7	9	6	$Ct^{3-}/(HCt^{2-} + H_2Ct^{-})$

1 The solution of $NiCl_2$, and TSC mixture.
2 The solution of $NiCl_2$, TSC, and $NaBH_4$ mixture.
3 The solution of $NiCl_2$, TSC, $NaBH_4$, and H_2PdCl_4 mixture.
B Before injection of H_2PdCl_4.
A After injection of H_2PdCl_4.

combine with O_2 from air to form an oxidative etchant for the Ni core resulting in the formation of hollow NPs [52]. In an effort to understand how the core–shell NiPd NPs evolved into hollow spheres, time-resolved TEM analysis was carried out at aging times of 6 h (Fig. S11A) and 12 h (Fig. S11B) confirming that the formation of the hollow structure is a stepwise process. Oxidative etching started with local pitting on the surface of the solid NPs followed by the gradual dissolution of the Ni core generating a hollow structure with a rough shell having a thickness of 6.5 ± 1.8 nm (Fig. S11C). As the Cl^-/O_2 oxidative pair had the ability to also etch Pd, longer aging times resulted in smoothing of the shell to a thickness of 2.5 ± 0.5 nm (Fig. S4B). The etching ability of the Cl^-/O_2 pair is influenced by the pH of the solution as the oxidative strength of O_2 is significantly enhanced under acidic conditions [53]. To further understand the role of the Cl^- concentration, and pH in the etching mechanism of the core–shell NiPd NPs to form hollow NPs, the synthesis was carried out replacing HCl with NaCl, keeping the total Cl^- concentration equal to that of the 5 mM HCl solution. TEM analysis (Fig. S12) showed limited etching of the core–shell NPs after 24 h of aging, indicating that a combined effect of Cl^- ions and low pH was essential to achieve the shape transition from core-shell NPs to hollow NPs.

When using a Pd precursor solution with a higher HCl concentration, *i.e.* H_2PdCl_4/10 mM HCl solution, aging resulted in the evolution from wormlike nanowire networks to nanodendrites. As previously described, EDX analysis revealed that the composition of the nanowires consisted of NiPd alloy regions and Pd regions. The nanodendrites produced on aging were composed primarily of Pd with trace amounts of Ni detected by EDX and XPS analysis. The high density of defect sites at the particle–particle interface on the nanowires is susceptible to oxidative etching from Cl^-/O_2. Faster etching of the NiPd regions resulted in the breakage of the extended nanowire network (Fig. S13. A, B). Pd NPs aggregation driven by the diffusion-controlled deposition and surface energy minimization results in the formation of nanodendrites [54–57].

We further investigated the use of other first-row transition metal seeds in the shape evolution of Pd-based bimetallic NPs. Co-Pd, Fe-Pd, and Cu-Pd systems were investigated by changing the metal precursors (see Experimental section for details). As shown in Figs. S14, S15, and S16, under low HCl concentration (H_2PdCl_4/5 mM HCl solution) core–shell structures could not be formed when Ni^{2+} was substituted by equal molar amounts of Co^{2+}, Fe^{3+}, and Cu^{2+}. In comparison, using a higher HCl concentration (H_2PdCl_4/10 mM HCl solution) showed the same trend in the shape evolution of forming nanowires and nanodendrites on aging, thus this methodology appears to have wider applicability to other Pd-metal systems. The switch of metal from Ni to Co, Fe, and Cu involved changes to several parameters, including the redox potential of metal ions, the binding strength of the capping agent, and the degree of lattice mismatch between these metals and Pd.

3.2. Catalytic activity of nanostructures

The catalytic efficiency of NPs is strongly dependent on their composition, size and morphology [58]. Hence, the catalytic performance of the obtained NiPd NPs with different structures was evaluated using hydrogenation of 4-nitrophenol (4-NP) to 4-aminophenol (4-AP) in the presence of $NaBH_4$ as a model reaction system. The four nanostructures, core–shell, hollow, nanowire networks and nanodendrites, were supported on acid-treated activated carbon (AC) with a Pd metal loading determined by ICP-OES as shown in Table 2.

The conversion of 4-nitrophenolate ion to 4-AP was monitored by UV–Vis spectroscopy through the disappearance of the 4-NP absorbance peak at 400 nm, which is accompanied by the gradual appearance of a new peak at 312 nm representing the formation of 4-AP [59,60]. Figs. 6, S17 exhibits the time-dependent UV–Vis absorption spectra assessing the catalytic activity of core–shell NPs, hollow NPs, nanowire networks, nanodendrites structures and commercial Pd/C for 4-nitrophenol reduction. The corresponding linear plots of normalized absorbance $-\ln(A_t/A_0)$ of the 4-nitrophenolate ions at 400 nm versus reaction time are also shown. With the exception of the nanodendrite catalyst, all the other catalyst morphologies displayed a short induction period (~30 s) associated with the adsorption of the reactant species on the catalyst surface. The reduction reaction obeyed pseudo-first-order kinetics with respect to the concentration of 4-NP as $NaBH_4$ was used in excess in the reaction. From eq.: $[-\ln(A_t/A_0) = K_{app}\ t]$ where A_t and A_0 are the absorbance of the 4-nitrophenolate ions at 400 nm at time t and at 0 *sec*, respectively. The value of the apparent rate constant (K_{app}) was obtained from the slopes of the best-fit lines (excluding the t_{ind} region). A comparison of the catalytic

Table 2
Comparison of catalytic properties of different nanostructures supported on AC and commercial Pd/C.

Conc. of HCl	Catalyst	Pd content (X 10^{-3} mg/mg)	K_{app} (X 10^{-3} s^{-1})	Normalized rate constant K_{nor}	
		Pd		Pd-$mg^{-1}.s^{-1}$	Pd-$mmol^{-1}.s^{-1}$
5 mM HCl	Core-shell NPs/AC	6.63[a]	7.80	1.1765	125.201
	Hollow NPs/AC	3.99[a]	3.97	0.9950	105.886
10 mM HCl	Nanowire networks/AC	21.12[a]	6.68	0.3163	33.652
	Nanodendrites/AC	14.28[a]	10.98	0.7689	81.824
	Commercial Pd/C	50	9.28	0.1856	19.753

[a] Pd content measured by ICP-OES.

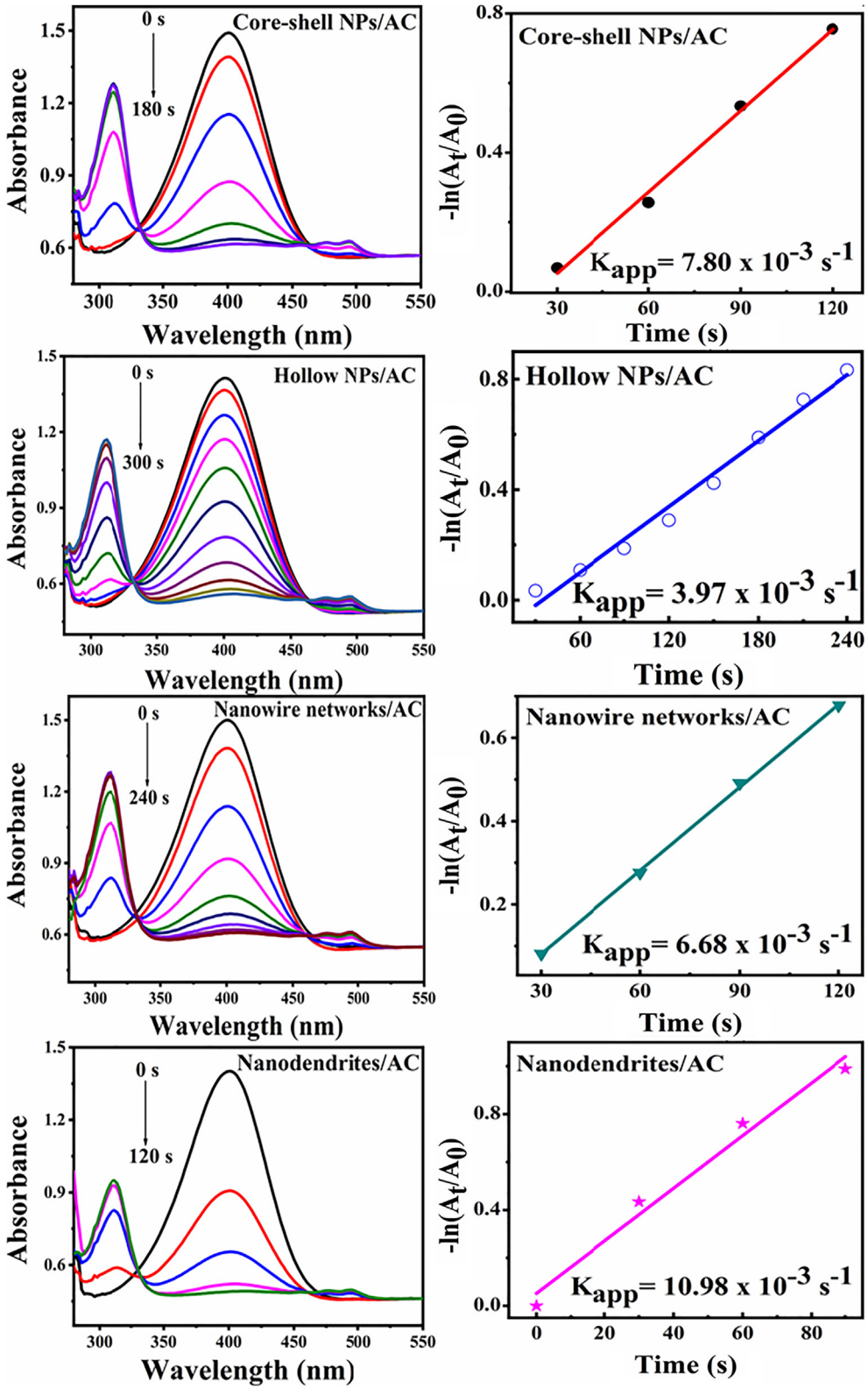

Fig. 6. Representative time-dependent absorption spectra showing the reduction of 4-NP to 4-AP using the four nanostructures supported on AC and their corresponding normalized absorbance of the 4-NP at 400 nm versus reaction time.

reaction rates of the different nanostructures and commercial Pd/C is summarized in Table 2. The mass normalized rate constants of the nanostructures were all higher than that of commercial Pd/C. The core shell NPs displayed 6 times the activity demonstrating the increased utilization efficiency associated with the Pd located only on the shell. Similarly, the hollow NPs displayed over five time the mass normalized rate, attributed to increased surface area in the hollow interior.

For nanostructures prepared using the H_2PdCl_4/5 mM HCl solution, a comparison of the rate constants normalized to the Pd content show that the core–shell structures displayed slightly better catalytic activity than that of the hollow structures, which can be attributed to the synergistic alloy effect and the lattice strain effect created between the core and shell [61,62]. In the case of using the H_2PdCl_4/10 mM HCl solution, the nanodendrites showed superior catalytic activity. The mass normalized rate coefficient of the nanodendrites was 2.4 times greater than that of the nanowire networks. Despite, the excellent catalytic efficiency of nanowire networks previously reported [63,64] owing to their unique anisotropic structures, they exhibited the lowest catalytic performance in our study compared to other morphologies. The open structure of the nanowire networks and unfavourable interactions with the activated carbon support may hinder reactivity. All nanostructures catalysed the reaction to completion in very short reaction times. The existence of an electronic effect, confirmed by the observed shift in the B.E. of the Pd 3d doublet, promotes the adsorption of hydrogen onto the catalyst surface and facilitates the electron transfer from $NaBH_4$ to 4-NP [59,65]. Table S1 provides details on literature reports using this catalytic reaction.

4. Conclusions

In summary, we have achieved the shape-controlled synthesis of NiPd bimetallic NPs by simply tuning the HCl concentration in the H_2PdCl_4 solution and by the reaction aging time. While $NaBH_4$ is conventionally regarded as a strong reducing agent resulting in the rapid reduction of the metal precursor, we demonstrate that modulation of the pH can alter the reducing power of $NaBH_4$ allowing different NP morphologies to be easily synthesized under aqueous and ligand-free environment. The NiPd core–shell nanostructures could be assigned to quenching of the GRR between Ni NPs and H_2PdCl_4 through enhanced reduction power of $NaBH_4$. Simple aging of these NPs in solution results in the formation of hollow Pd NPs due to the oxidative etching of the Ni core. Conducting the reaction at a higher concentration of HCl gave rise to worm-like nanowire networks which extended for hundreds of nanometers. The formation of these 2D architectures formed at a lower pH was attributed to the enhanced reduction rate of the Pd precursor, insufficient capping of citrate ions and low surface charge of the NPs formed at the early stage. Subsequent aging of these nanowire networks results in the formation of Pd nanodendrites due to the oxidative etching of Ni, followed by the self-aggregation of small NPs through the diffusion-limited mechanism generating the dendritic structure. Therefore in this study, the concentration of HCl in the Pd precursor (H_2PdCl_4) exhibited a significant role in tailoring the structure of NiPd bimetallic NPs and provides new insights into the growth mechanism when using $NaBH_4$ as a reducing agent. The ability to rapidly synthesize nanostructures with diverse morphology and dimensionality is highly advantageous to catalytic and electrocatalytic applications.

CRediT authorship contribution statement

Mai Maize: Conceptualization, Methodology, Formal analysis, Investigation, Writing - original draft, Funding acquisition. **Hanaa A. El-Boraey:** Writing - review & editing. **Mohamed I. Ayad:** Writing - review & editing. **Justin D. Holmes:** Conceptualization, Writing - review & editing, Supervision, Visualization, Funding acquisition, Supervision. **Gillian Collins:** Conceptualization, Writing - review & editing, Visualization, Funding acquisition, Supervision.

Declaration of Competing Interest

The authors declare that they have no known competing financial interests or personal relationships that could have appeared to influence the work reported in this paper.

Acknowledgements

This study was funded by the Egyptian government, Ministry of Higher Education, Cultural Affairs and Missions Sector and Science Foundation Ireland (Grant No.: 12-RC-2278 P2). We also gratefully acknowledge the Egyptian Bureau for Cultural & Educational Affairs, Egyptian Embassy in London.

Appendix A. Supplementary material

Supplementary data to this article can be found online at https://doi.org/10.1016/j.jcis.2020.10.030.

References

[1] Y. Xia et al., Shape-controlled synthesis of metal nanocrystals: simple chemistry meets complex physics?, Angew. Chem. Int. Ed. 48 (1) (2009) 60–103.
[2] D. Wang, Y. Li, Bimetallic nanocrystals: liquid-phase synthesis and catalytic applications, Adv. Mater. 23 (9) (2011) 1044–1060.
[3] K.D. Gilroy et al., Bimetallic nanocrystals: syntheses, properties, and applications, Chem. Rev. 116 (18) (2016) 10414–10472.
[4] O.M. Wilson et al., Effect of Pd nanoparticle size on the catalytic hydrogenation of allyl alcohol, J. Am. Chem. Soc. 128 (14) (2006) 4510–4511.
[5] N. Dimitratos, F. Porta, L. Prati, Au, Pd (mono and bimetallic) catalysts supported on graphite using the immobilisation method, Appl. Catal. A Gen. 291 (1–2) (2005) 210–214.
[6] I. Saldan et al., Chemical synthesis and application of palladium nanoparticles, J. M. Sci. 50 (6) (2015) 2337–2354.
[7] A. Chen, C. Ostrom, Palladium-based nanomaterials: synthesis and electrochemical applications, Chem. Rev. 115 (21) (2015) 11999–12044.
[8] J. Gu, Y.-W. Zhang, F.F. Tao, Shape control of bimetallic nanocatalysts through well-designed colloidal chemistry approaches, Chem. Soc. Rev. 41 (24) (2012) 8050–8065.
[9] P. Xi et al., Facile synthesis of Pd-based bimetallic nanocrystals and their application as catalysts for methanol oxidation reaction, Nanoscale 5 (13) (2013) 6124–6130.
[10] A.K. Singh, Q. Xu, Synergistic catalysis over bimetallic alloy nanoparticles, ChemCatChem 5 (3) (2013) 652–676.
[11] L. Feng et al., Pd–Ni alloy nanoparticles as effective catalysts for Miyaura-Heck coupling reactions, J. Phys. Chem. C 119 (21) (2015) 11511–11515.
[12] K. Seth, P. Purohit, A.K. Chakraborti, Cooperative catalysis by palladium-nickel binary nanocluster for Suzuki-Miyaura reaction of ortho-heterocycle-tethered sterically hindered aryl bromides, Org. Lett. 16 (9) (2014) 2334–2337.
[13] R.K. Rai et al., Access to highly active Ni–Pd bimetallic nanoparticle catalysts for C-C coupling reactions, Catal. Sci. Technol. 6 (14) (2016) 5567–5579.
[14] M. Wang et al., PdNi hollow nanoparticles for improved electrocatalytic oxygen reduction in alkaline environments, ACS Appl. Mater. Interfaces 5 (23) (2013) 12708–12715.
[15] Y. Feng et al., Surface-modulated palladium-nickel icosahedra as high-performance non-platinum oxygen reduction electrocatalysts, Sci. Adv. 4 (7) (2018) eaap8817.
[16] M. Ren et al., Lattice contracted Pd-hollow nanocrystals: Synthesis, structure and electrocatalysis for formic acid oxidation, J. Power Sources 246 (2014) 32–38.
[17] K. Mori et al., Synergic catalysis of PdCu alloy nanoparticles within A macroreticular basic resin for hydrogen production from formic acid, Chem. Eur. J. 21 (34) (2015) 12085–12092.
[18] Z. Wu, S. Yang, W. Wu, Shape control of inorganic nanoparticles from solution, Nanoscale 8 (3) (2016) 1237–1259.
[19] J. Watt, S. Cheong, R.D. Tilley, How to control the shape of metal nanostructures in organic solution phase synthesis for plasmonics and catalysis, Nano Today 8 (2) (2013) 198–215.
[20] C. Burda et al., Chemistry and properties of nanocrystals of different shapes, Chem. Rev. 105 (4) (2005) 1025–1102.
[21] G. Collins, J.D. Holmes, Engineering metallic nanoparticles for enhancing and probing catalytic reactions, Adv. Mater. 28 (27) (2016) 5689–5695.
[22] Y. Xia, X. Xia, H.C. Peng, Shape-controlled synthesis of colloidal metal nanocrystals: thermodynamic versus kinetic products, J. Am. Chem. Soc. 137 (25) (2015) 7947–7966.
[23] J. Xiang et al., Bimetallic Pd-Ni core-shell nanoparticles as effective catalysts for the Suzuki reaction, Nano Res. 7 (9) (2014) 1337–1343.

[24] Ö. Metin et al., Ni/Pd core/shell nanoparticles supported on graphene as a highly active and reusable catalyst for Suzuki-Miyaura cross-coupling reaction, Nano Res. 6 (1) (2012) 10–18.
[25] Q. Wang et al., Triple-enzyme mimetic activity of nickel-palladium hollow nanoparticles and their application in colorimetric biosensing of glucose, Chem. Commun. 52 (31) (2016) 5410–5413.
[26] Y. Sun, B.T. Mayers, Y. Xia, Template-engaged replacement reaction: A one-step approach to the large-scale synthesis of metal nanostructures with hollow interiors, Nano Lett. 2 (5) (2002) 481–485.
[27] X. Xia et al., 25th anniversary article: galvanic replacement: a simple and versatile route to hollow nanostructures with tunable and well-controlled properties, Adv. Mater. 25 (44) (2013) 6313–6333.
[28] Y. Yang et al., Galvanic replacement-free deposition of Au on Ag for core-shell nanocubes with enhanced chemical stability and SERS activity, J. Am. Chem. Soc. 136 (23) (2014) 8153–8156.
[29] T. Fu et al., Hollow porous nanoparticles with Pt skin on a Ag–Pt alloy structure as a highly active electrocatalyst for the oxygen reduction reaction, J. Mater. Chem. A 4 (22) (2016) 8803–8811.
[30] G. Prieto et al., Hollow nano- and microstructures as catalysts, Chem. Rev. 116 (22) (2016) 14056–14119.
[31] X. Huang et al., High density catalytic hot spots in ultrafine wavy nanowires, Nano Lett. 14 (7) (2014) 3887–3894.
[32] Y. Imura et al., Preparation and catalytic activity of Pd and bimetallic Pd-Ni nanowires, Langmuir 30 (17) (2014) 5026–5030.
[33] H. Liu et al., Probing ultrathin one-dimensional Pd–Ni nanostructures as oxygen reduction reaction catalysts, ACS Catal. 4 (8) (2014) 2544–2555.
[34] J.-N. Zheng et al., A facile general strategy for synthesis of palladium-based bimetallic alloyed nanodendrites with enhanced electrocatalytic performance for methanol and ethylene glycol oxidation, J. Mater. Chem. A 2 (32) (2014) 12899–12906.
[35] H. Kilic et al., Monodisperse Ni@Pd Core@Shell Nanoparticles Assembled On Reduced Graphene Oxide As A Highly Efficient And Reusable Heterogeneous catalyst for the C-H bond arylation of imidazo[1,2-a]pyridine with aryl halides, ACS Sustain. Chem. Eng. 6 (9) (2018) 11433–11440.
[36] L. Chen et al., Nanoporous PdNi bimetallic catalyst with enhanced electrocatalytic performances for electro-oxidation and oxygen reduction reactions, Adv. Funct. Mater. 21 (22) (2011) 4364–4370.
[37] S. Murugesan, V. Subramanian, Effects of acid accelerators on hydrogen generation from solid sodium borohydride using small scale devices, J. Power Sources 187 (1) (2009) 216–223.
[38] U.B. Demirci, P. Miele, Cobalt in NaBH4 hydrolysis, Phys. Chem. Chem. Phys. 12 (44) (2010) 14651–14665.
[39] L. Kvitek, et al., Physicochemical Aspects of Metal Nanoparticle Preparation. Silver Nanoparticles - Health and Safety [Working Title] 2019; Available from: https://www.intechopen.com/online-first/physicochemical-aspects-of-metal-nanoparticle-preparation.
[40] M. Wojnicki et al., Kinetics of palladium(II) chloride complex reduction in aqueous solutions using dimethylamineborane, Hydrometallurgy 110 (1–4) (2011) 56–61.
[41] M. Wojnicki, K. Fitzner, M. Luty-Blocho, Kinetic studies of nucleation and growth of palladium nanoparticles, J. Colloid Interface Sci. 465 (2016) 190–199.
[42] J.M. van Middlesworth, S.A. Wood, The stability of palladium(II) hydroxide and hydroxy–chloride complexes: an experimental solubility study at 25–85 °C and 1 bar, Geochim. Cosmochim. Acta 63 (11–12) (1999) 1751–1765.
[43] L. Pei, K. Mori, M. Adachi, Formation process of two-dimensional networked gold nanowires by citrate reduction of AuCl4- and the shape stabilization, Langmuir 20 (18) (2004) 7837–7843.
[44] X. Ji et al., Size control of gold nanocrystals in citrate reduction: the third role of citrate, J. Am. Chem. Soc. 129 (45) (2007) 13939–13948.
[45] H. Tyagi et al., A facile pH controlled citrate-based reduction method for gold nanoparticle synthesis at room temperature, Nanoscale Res. Lett. 11 (1) (2016) 362.
[46] K.D. Gilroy et al., Sacrificial templates for galvanic replacement reactions: design criteria for the synthesis of pure Pt nanoshells with a smooth surface morphology, Chem. Mater. 26 (10) (2014) 3340–3347.
[47] J. Wang et al., Synthesis of Pd nanowire networks by a simple template-free and surfactant-free method and their application in formic acid electrooxidation, Electrochem. Commun. 12 (2) (2010) 219–222.
[48] Z. Tang, N.A. Kotov, M. Giersig, Spontaneous organization of single CdTe nanoparticles into luminescent nanowires, Science 297 (5579) (2002) 237–240.
[49] P. Qiu, C. Mao, Seed-mediated shape evolution of gold nanomaterials: from spherical nanoparticles to polycrystalline nanochains and single-crystalline nanowires, J. Nanopart. Res. 11 (4) (2008) 885–894.
[50] Y. Sun, B. Mayers, Y. Xia, Transformation of silver nanospheres into nanobelts and triangular nanoplates through a thermal process, Nano Lett. 3 (5) (2003) 675–679.
[51] H. Zhang, D. Wang, Controlling the growth of charged-nanoparticle chains through interparticle electrostatic repulsion, Angew. Chem. Int. Ed. 47 (21) (2008) 3984–3987.
[52] Y. Xiong et al., Corrosion-based synthesis of single-crystal Pd nanoboxes and nanocages and their surface plasmon properties, Angew. Chem. Int. Ed. 44 (48) (2005) 7913–7917.
[53] Y. Xiong et al., Kinetically controlled synthesis of triangular and hexagonal nanoplates of palladium and their SPR/SERS properties, J. Am. Chem. Soc. 127 (48) (2005) 17118–17127.
[54] F. Wang et al., Porous single-crystalline palladium nanoparticles with high catalytic activities, Angew. Chem. Int. Ed. 51 (20) (2012) 4872–4876.
[55] J. Wang et al., One-step and rapid synthesis of "clean" and monodisperse dendritic Pt nanoparticles and their high performance toward methanol oxidation and p-nitrophenol reduction, Nanoscale 4 (5) (2012) 1549–1552.
[56] W. Wang et al., Pt-Ni nanodendrites with high hydrogenation activity, Chem. Commun. 49 (28) (2013) 2903–2905.
[57] B. Lim, Y. Xia, Metal nanocrystals with highly branched morphologies, Angew. Chem. Int. Ed. 50 (1) (2011) 76–85.
[58] W. Zhang et al., Facile, template-free synthesis of silver nanodendrites with high catalytic activity for the reduction of p-nitrophenol, J. Hazard. Mater. 217–218 (2012) 36–42.
[59] T.A. Revathy et al., Pulsed electrodeposited dendritic Pd-Ni alloy as a magnetically recoverable nanocatalyst for the hydrogenation of 4-nitrophenol, J. Alloys Compd. 735 (2018) 1703–1711.
[60] T.A. Revathy et al., Highly active graphene-supported palladium-nickel alloy nanoparticles for catalytic reduction of 4-nitrophenol, Appl. Surf. Sci. 449 (2018) 764–771.
[61] D. Chen et al., Gold-catalyzed formation of core–shell gold–palladium nanoparticles with palladium shells up to three atomic layers, J. Mater. Chem. A 4 (10) (2016) 3813–3821.
[62] B.T. Sneed, A.P. Young, C.-K. Tsung, Building up strain in colloidal metal nanoparticle catalysts, Nanoscale 7 (29) (2015) 12248–12265.
[63] X. Yu et al., Pt-M (M = Cu Co, Ni, Fe) nanocrystals: from small nanoparticles to wormlike nanowires by oriented attachment, Chem. Eur. J. 19 (1) (2013) 233–239.
[64] D. Sun et al., General synthetic protocol for the synthesis of Ru-X (X=Rh, Pd, Ag) heterogeneous ultrathin nanowires with a tunable composition, ChemCatChem 9 (2) (2017) 347–353.
[65] T.R. Silva et al., The catalytic evaluation of bimetallic Pd-based nanocatalysts supported on ion exchange resin in nitro and alkyne reduction reactions, New J. Chem. 43 (18) (2019) 7083–7092.